

PMT Signal Processing

Bouke Jung (bjung@nikhef.nl)

November 4, 2021

Abstract

This document outlines models used to describe PMT data and the routines for calibrating the PMT as seen from a Jpp perspective.

1 Introduction

The cubic kilometer neutrino telescope (KM3NeT) forms a research infrastructure, consisting of large 3D-arrays of photomultiplier tubes deployed in the deep waters of the Mediterranean Sea. It allows for the detection of neutrinos by recording the arrival times of Cherenkov photons produced by the relativistic charged particles which emerge from a neutrino interaction.

To reconstruct neutrino events, one needs to analyze the time-position correlations between photomultiplier tube hits. This can be done using a software structure called Jpp (pronounced as yi-pee-pee). This document presents the functionalities incorporated in two C++ classes (JPMTSignalProcessorInterface and JPMTAnalogueSignalProcessor), which simulate the response of a single photomultiplier tube to photon hits.

2 The Photomultiplier Tube

The photomultiplier tube (PMT) constitutes the principal sensor of KM3NeT. Sporting a development history of over 90 years [1], their fundamental working principle has remained the same over time. In this section we explain how a photomultiplier tube functions from a hardware perspective. We also discuss the model used to describe a photomultiplier tube's response to an incoming light signal.

The base design of a photomultiplier tube consists of four consecutively placed elements, encapsulated by a vacuum tube. These are the photo-cathode, the focusing electrodes, the electron multiplier and the anode. When combined, they allow for the conversion of individual photons on one end of the device into measurable currents on the other. In figure 1 sketches the overall detection principle is sketched. External light enters the vacuum tube through an input window located at the front. The light subsequently impinges on the photo-cathode surface, where an electron can be emitted into the vacuum through the photoelectric effect. A focusing electrode accelerates and focuses the electron towards the electron multiplier. This is a system consisting of several secondary-emission electrodes, called dynodes, which iteratively multiply the number of primary electrons originating from the photo-cathode, so that a measurable current at the anode is produced. A voltage divider supplies the electric fields needed to accelerate and focus the output electrons from one dynode to the next.

The material and structural design of a photomultiplier tube can be adjusted to satisfy specific needs and intents. In KM3NeT the list of specifications includes a high efficiency to detect light of the quantum level with nanosecond time resolution. Taking this into account, the collaboration decided to use the R12199-02 type PMT produced by Hamamatsu.

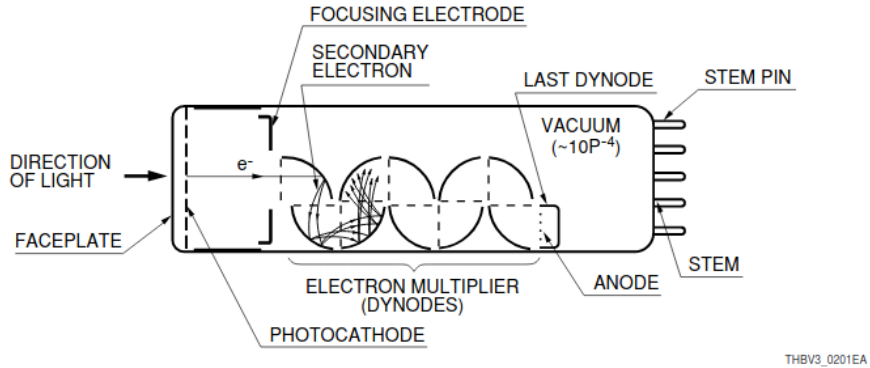


Figure 1: A schematic overview of the principal building blocks comprising a photomultiplier tube (from [2]).

2.1 Characteristic Variables

The quantity that determines the light sensitivity of a PMT is referred to as the quantum efficiency (QE). It is defined as the probability that an incoming photon is converted into a primary electron. Depending upon which material is used to coat the photo-cathode, the quantum efficiency of the photomultiplier tube will peak at different frequencies. For the R12199-02 type PMTs developed for KM3NeT, this coating material is Bialkali (SbKCs). Figure 2 shows the resulting quantum efficiency of the PMT as a function of the wavelength of incident light.

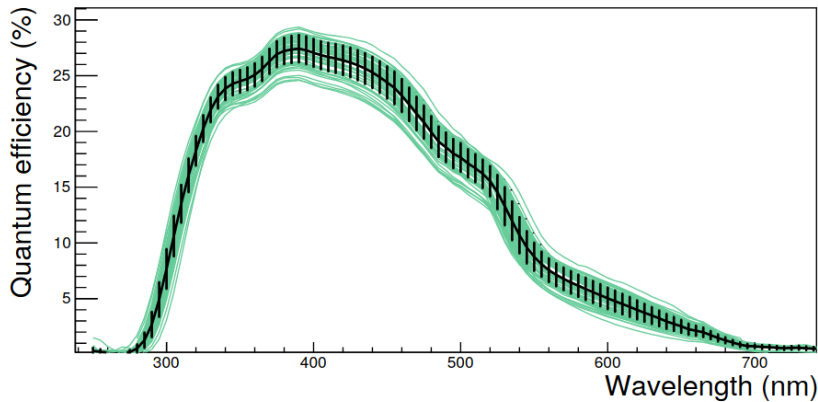


Figure 2: The photo-cathode quantum efficiency as a function of the wavelength, as measured for 56 R12199-02 type PMTs (from [3]).

Not all photo-electrons generated at the photo-cathode or in the dynodes result in effective secondary emission in the subsequent stages of the electron multiplier. For example, certain trajectories may be diverted such that a following dynode is missed. Effects like these are summarized in a quantity referred to as the collection efficiency, n . In principle, each inter-dynode space is characterized by its own collection efficiency, n_i . However, these can generally not be characterized individually. Instead, we multiply the collection efficiencies of all dynode stages with their respective secondary emission coefficients, ϵ_i , to define an overall electron multiplication factor called the gain:

$$G = \prod_{i=1}^N n_i \epsilon_i \quad (1)$$

In general it is useful to define the gain in terms of the high voltage applied to the dynode stages. The dependence of the secondary emission coefficients on the inter-dynode voltages, V_i , is generally well-described by a power-law [4]:

$$\epsilon_i = a V_i^k, \quad (2)$$

where a is a constant associated with the dynode material and where $k < 1$ accounts for losses (e.g. due to scattering). Assuming that the voltage is distributed uniformly over the inter-dynode stages, i.e. $V_i = \frac{V}{N+1}$, and that all secondary emission coefficients are identical ($\epsilon_i = \epsilon$), this leads to the following expression for the gain:

$$G \equiv n \cdot \epsilon^N = n \cdot \frac{a^N V^{kN}}{(N+1)^{kN}} = A \cdot V^{kN}, \quad (3)$$

where we have substituted the definition $A \equiv n \cdot a^N (N+1)^{-kN}$, with $n = \prod_{i=1}^N n_i$, in the last step. Due to the statistical behavior of the electron multiplication process, the overall gain of a photomultiplier tube exhibits a spread. To good approximation, we can describe this spread by regarding the secondary emissions at each dynode as individual Poisson processes, having means $\lambda_i = n_i \epsilon_i$ and standard deviations $\sigma_i \equiv \sqrt{\lambda_i} = \sqrt{n_i \epsilon_i}$. If we follow this line of reasoning, we obtain a gain for the overall electron multiplication given by equation 1, whilst we retrieve a variance equal to [5; 6]:

$$\Sigma^2 = \sum_{i=1}^N \left(\frac{\sigma_i}{\lambda_i} \right)^2 \cdot \frac{\prod_{j=1}^N \lambda_j^2}{\prod_{k=1}^{i-1} \lambda_k} = \sum_{i=1}^N \frac{1}{n_i \epsilon_i} \cdot \frac{\prod_{j=1}^N (n_j \epsilon_j)^2}{\prod_{k=1}^{i-1} n_k \epsilon_k}. \quad (4)$$

In other words, we obtain a relative variance:

$$\left(\frac{\Sigma}{G} \right)^2 = \sum_{i=1}^N \left(\prod_{j=1}^i n_j \epsilon_j \right)^{-1}, \quad (5)$$

Assuming that all secondary emission coefficients and collection efficiencies are roughly equal (i.e. $n_i \epsilon_i \approx n_1 \epsilon_1$), this can be reduced to $1/(n_1 \epsilon_1 - 1)$. Looking at equation 5, it becomes apparent that for $n_i \epsilon_i \gg 1$, any spread in the number of secondary electrons measured at the anode will be dominated by the variance in the yield of the first dynode. This can be thought of intuitively as a consequence of the limited statistics within the first multiplication stage.

Depending upon the choice of dynode material and structure, the values of the gain and the variance of the secondary electron distribution at the anode will change. Commonly used materials include AgMg, CuBe and NiAl [7]. Although these do not display substantial secondary emission by themselves, the oxidation products (e.g. MgO, BeO and Al₂O₃) forming on their surface do.

Where the dynode material influences the value of ϵ_i , its geometry holds sway over the collection efficiency, n_i . Two prevalent geometry choices are the Venetian blind and the box-and-grid structures. The first arranges the dynodes in parallel strips, rotated slightly with respect to the longitudinal axis of the tube. This type of geometry has high collection efficiency and good gain stability. However, its time resolution is rather poor [2], because the electric fields close to the surface of each dynode are small [7]. The same holds true for the box-and-grid structure, which implements dynodes cut in a cylindrical shape which are positioned in quadrants. Since the detection of individual Cherenkov photons requires a time resolution of 1 ns, neither the Venetian blind nor the box-and-grid structure would be a good design choice for KM3NeT. Instead, the Hamamatsu R12199-02 photomultipliers we use, contain a linear focusing structure, where all dynodes are

positioned in a row. Combined with the strong electric fields between each stage, this ensures that the transit-times of individual photo-electrons remains small, such that the required time resolutions can be achieved. A downside to this type of design is the relatively large non-uniformity of the photomultipliers response as function of incidence position and incidence angle on the photo-cathode. In the KM3NeT photomultiplier tubes, these effects lead to efficiency variations of 10% to 25% [8]. Other types of photomultipliers typically perform better in this respect, displaying efficiency variations of no more than 10% [9].

The time response of a photomultiplier tube is generally evaluated through something referred to as the transit-time distribution. This distribution maps out the time durations between the impingement of a photon on the photo-cathode and the appearance of an output current at the anode. It features a peak alongside contributions from prepulses and delayed pulses. The width of the peak is commonly referred to as the transit-time spread (TTS) and scales approximately with the number of primary photo-electrons per pulse, N_{pe} as $1/N_{pe}$. It has been estimated to be 3 ns for the photomultiplier tubes employed in KM3NeT [10]. The position of the peak in the transit time distribution relates to the voltage difference between the cathode and the anode, V , and is roughly proportional to $1/\sqrt{V}$. This follows from the acceleration of the photo-electrons across the electric fields.

To describe the temporal behavior of output currents generated by individual photon hits we generally refer to two quantities known as the current's rise-time and its decay-time. The rise-time corresponds to the time the associated analogue pulse takes to get from 10% to 90% of the maximal pulse height. Conversely, the decay-time is defined as the time to go back from 90% of the maximal pulse height to 10%. Whereas the rise-time is — to good approximation — independent of the number of photo-electrons, the decay-time generally increases with the number of generated primary photo-electrons. This is a consequence of the varying latencies of the secondary electrons and the relaxation time of the electronics.

3 Pulse shape modeling and time-over-threshold

The primary output of PMTs consist of currents, typically a few tens of ns in width, when a single photo-electron is produced. It is fed to an amplifier and subsequently passed through a threshold discriminator to cut out electronic noise. Typically, the threshold of a PMT corresponds to a 0.3 photo-electron signal. Both the leading and the trailing edge of the output of the threshold discriminator are timestamped. The least significant bit of these timestamps is 1 ns, which corresponds to a resolution of $1/\sqrt{12}$ ns. Once the timestamps have been applied, the identifier of the associated PMT, the arrival time of the signal, i.e. the leading edge, and the time-over-threshold are stored for future use. The value of the leading edge depends on the height of the pulse passed to the threshold discriminator. This effect is referred to as time-slewing.

To maximize the performance of the event reconstruction and to reproduce the key features of a PMT in the simulations, we need to be able to relate time-over-threshold values to the pulse-shapes which were originally recorded at each PMT. In Jpp this is done by assuming that all pulses follow the same, general shape consisting of a Gaussian with an exponential tail. The resulting output voltage for a nominal pulse, generated by a single photo-electron hit, can thus be written down as:

$$V(t) = \begin{cases} e^{-\frac{1}{2}\left(\frac{t}{\sigma}\right)^2}, & t \leq \tilde{t}, \\ \frac{1}{C}e^{\frac{t}{\tau}}, & t > \tilde{t}, \end{cases} \quad (6)$$

where t denotes the time measured with respect to the pulse maximum, C is a normalization constant, σ is the width of the Gaussian component of the pulse and τ is the decay-time associated with the exponential part. Note that the Gaussian width is related to the PMT rise-time as

$t_r = \sigma \left(\sqrt{-2 \ln(0.1)} - \sqrt{-2 \ln(0.9)} \right) \approx 1.69\sigma$. The time corresponding to the match point, \tilde{t} , is fixed by

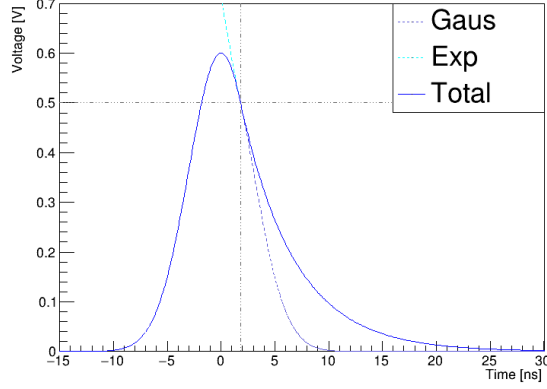


Figure 3: The model analogue pulse shape model, as described by equation 9). The match point between the Gaussian and exponential regime (c.f. equation 8), shown at the intersection of the black dotted lines, is found by imposing equal derivatives and function values.

requiring both the function values and the derivatives of the Gaussian and exponential to be equal. These constraints yield:

$$\tilde{t} = \frac{\sigma^2}{\tau}, \quad (7)$$

$$C \equiv V(\tilde{t}) = e^{-\frac{1}{2}\left(\frac{\tilde{t}}{\tau}\right)^2}. \quad (8)$$

We can now extrapolate the nominal single photo-electron pulse-shape to the voltage output of a general pulse by exploiting the linearity between pulse amplitude and total associated charge, q :

$$V(t, q) = \frac{q}{R} V(t), \quad (9)$$

where R is a constant related to the resistance of the electrical read-out circuit. Figure 3 shows an example analogue pulse with an amplitude of 0.6 V, comprising a Gaussian centered around the origin with a variance equal to 9.0 nanoseconds and an exponential decay time of 5.0 nanoseconds.

By inverting equation 6 we can express the relative time as function of pulse amplitude and determine an analytical expression for the time-over-threshold. Let us first define the leading and the trailing edge of a visible PMT hit, t_1 and t_2 , as the first and last time during which the corresponding pulse exceeds the voltage threshold V_0 :

$$t_1 = -\sigma \sqrt{2 \ln \left(\frac{q}{RV_0} \right)}, \quad (10)$$

$$t_2 = \begin{cases} \sigma \sqrt{2 \ln \left(\frac{q}{RV_0} \right)}, & V(\tilde{t}, q) \leq V_0, \\ \tau \ln \left(\frac{q}{C RV_0} \right), & V(\tilde{t}, q) > V_0. \end{cases} \quad (11)$$

The time-over-threshold, ΔT , can be defined as the difference between these two times:

$$\begin{aligned}\Delta T(q) &\equiv t_2 - t_1 \\ &= \begin{cases} 2\sigma\sqrt{\ln\left(2\frac{q}{q_0}\right)}, & q_0 < q \leq \frac{q_0}{CR}, \\ \tau \ln\left(\frac{q}{Cq_0}\right) + \sigma\sqrt{-2\ln\left(\frac{q}{q_0}\right)}, & q > \frac{q_0}{CR}, \\ 0, & q \leq q_0, \end{cases} \end{aligned} \quad (12)$$

where we have substituted $V(\tilde{t}, q) = \frac{q}{R}V(\tilde{t}) = \frac{q}{R}C$ and introduced the threshold-equivalent charge, q_0 , set by the condition $V(0, q_0) = V_0$. Given that a nominal pulse corresponds to a time-over-threshold, $\Delta T(1)$, of 25.08 ns, we can relate the rise- and decay-time to each other, which reduces the total number of degrees of freedom in equation 12 to two (i.e. the Gaussian width, σ , and the threshold-setting, q_0) [11]. Starting from the case $q > \frac{q_0}{CR}$ and filling in $q = 1$ and $C = e^{-\left(\frac{\sigma}{\tau}\right)^2}$, we get:

$$\tau = \frac{-b + \sqrt{b^2 + 4\sigma^2 \ln(q_0)}}{2 \ln(q_0)}, \quad (13)$$

where we've substituted $b \equiv \sigma\sqrt{2 \ln(q_0)} - \Delta T(1)$.

Sometimes an analogue signal exceeds the voltage bias inside the amplifier and discriminator. In such scenarios the top part of the pulse will be clipped. This introduces a sub-regime to the case $q > \frac{q_0}{CR}$ in equation 12, where the time-over-threshold scales linearly with respect to charge as long as the pulse is in excess of the voltage bias:

$$\Delta T(q) = \tau \ln\left(\frac{q_L}{q_0 C}\right) + \sigma\sqrt{2\left(\frac{q_L}{q_0}\right)} + \beta(q - q_L), \quad q > q_L. \quad (14)$$

Here, β denotes the slope associated with the linear behavior, whereas q_L indicates the boundary between the linear and non-linear regime. Lab studies have pointed out that $\beta \approx 7.0 \text{ ns p.e.}^{-1}$ under normal PMT operation (i.e. with a high-voltage setting resulting in a current amplification of 3.45×10^6 [10]).

The linear behavior holds relatively well up to approximately 30 photo-electrons. Above this level, we observe a saturation effect, which causes a flattening of the time-over-threshold with increasing charge [12]. We model this effect phenomenologically with an inverse square-root modulation defined as:

$$f(\Delta T) = \frac{\Delta T_{\max}}{\sqrt{\Delta T_{\max}^2 + \Delta T^2}}, \quad (15)$$

where ΔT stands for the time-over-threshold without saturation and where $\Delta T_{\max} = 210 \text{ ns}$ is a constant which has been determined in the lab. Summarizing all of the above, we can write down the final expression for the time-over-threshold as a function of charge as:

$$\Delta \tilde{T} = \frac{\Delta T_{\max}}{\sqrt{\Delta T_{\max}^2 + \Delta T^2(q)}} \cdot \Delta T(q), \quad (16)$$

with:

$$\Delta T(q) = \begin{cases} 2\sigma\sqrt{-2\ln\left(\frac{q_0}{q}\right)}, & q_0 < q \leq \frac{q_0}{CR}, \\ \tau \ln\left(\frac{q}{q_0 \cdot C}\right) + \sigma\sqrt{2\ln\left(\frac{q}{q_0}\right)}, & \frac{q_0}{CR} < q \leq q_L, \\ \tau \ln\left(\frac{q_L}{q_0 \cdot C}\right) + \sigma\sqrt{2\ln\left(\frac{q_L}{q_0}\right)} + \beta(q - q_L), & q > q_L \\ 0, & q \leq q_0. \end{cases} \quad (17)$$

Figure 4 shows the full functional behavior of the time-over-threshold in terms of charge, as described by equation 16.

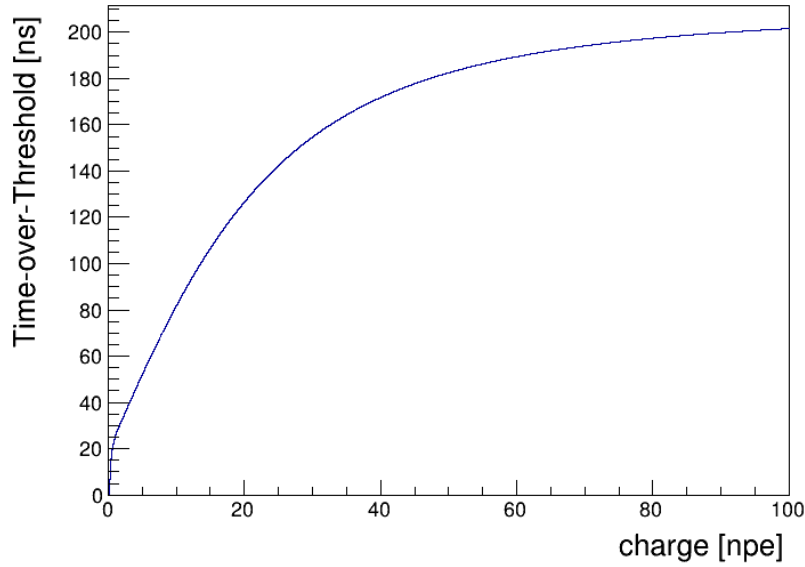


Figure 4: The time-over-threshold as function of charge, as described by equation 16.

Since the conversion described by equation 17 is one-to-one, we can directly set up its inverse to get the charge as function of time-over-threshold. Using equation 16 to convert between saturated and non-saturated time-over-threshold, this yields the following expression:

$$q(\Delta T) = \begin{cases} q_0 \cdot \exp\left[\frac{1}{8}\left(\frac{\Delta T}{\sigma}\right)^2\right], & 0 < \Delta T \leq \Delta T\left(\frac{q_0}{CR}\right), \\ q_0 \cdot \exp\left[\frac{z^2}{2}\right], & \Delta T\left(\frac{q_0}{CR}\right) < \Delta T \leq \Delta T(q_L), \\ q_L + \frac{1}{\beta}(\Delta T - \Delta T(q_L)), & \Delta T > \Delta T(q_L), \end{cases} \quad (18)$$

where we have defined $z \equiv \frac{-\sigma + \sqrt{\sigma^2 + 2\tau(\Delta T + \tau \ln(C))}}{\tau}$. In the following sections we will examine how frequently pulses with specific charge and time-over-threshold occur. For convenience, we will drop the tilde-notation, writing down the time-over-threshold variable including saturation as ΔT from this point onwards.

4 The Charge Distribution

For a given PMT it is possible to construct what is called the charge distribution by mapping out the occurrence frequencies of signals with different charges. When associated with physical light sources that give rise to the emission of single photo-electrons from the PMT's photo-cathode, the resulting histogram is called the single photo-electron distribution.

To infer the properties of light sources from data acquired with photomultiplier tubes, accurate modeling of each of the devices' single photo-electron distributions is paramount. In an ideal scenario, the output current at the anode would perfectly reflect the Poisson statistics governing the electron multiplication at each dynode stage. However, certain processes in between the dynode stages can give rise to disturbances. In the literature one therefore encounters other functions to describe the single photo-electron response, which allow for a more tunable variance. These range from a single Gaussian approximation [13], to log-normal [14] and negative binomial distributions [15; 16]. The single Gaussian approximation is adequate in cases where signal contributions deriving from underamplification and noise effects can be neglected. However, when these need to be taken into account the negative binomial and the log-normal are more suitable, since they accommodate an adjustable skewness. On the downside, they are computationally very difficult to manipulate.

Another solution for modeling underamplification consists of adding various distributions together. In KM3NeT, we have opted for the latter and modeled the full single photo-electron response of the PMTs as a mixture of two Gaussian distributions:

$$f(q; 1) = p \cdot \mathcal{G}(q; \mu_u, \sigma_u^2) + (1 - p) \cdot \mathcal{G}(q; G, \Sigma^2), \quad (19)$$

where p corresponds to the occurrence probability of an underamplified hit and $\mathcal{G}(x; \mu, \sigma^2)$ to a Gaussian distribution with a mean μ and standard deviation σ . The mean and standard deviation of the nominal (underamplified) distribution are referred to as G and Σ (μ_u and σ_u), respectively. These parameters are related by the expression $\Sigma = \sigma_G \sqrt{G}$, where G and σ_G correspond to the gain and the gainspread of the PMT. By convoluting the single photo-electron distribution N times with itself, we retrieve the multi photo-electron distribution, generated by N primary electrons at the photo-cathode:

$$\begin{aligned} f(q; N) &\equiv f(q; N - 1) \otimes f(q; 1) \\ &= \sum_{k=0}^N \binom{N}{k} p^{N-k} (1-p)^k \cdot \mathcal{G}(q; \mu_k, \sigma_k^2), \end{aligned} \quad (20)$$

where $\mu_k \equiv (N - k)\mu_u + kG$ and $\sigma_k \equiv \sqrt{(N - k)\sigma_u^2 + k\Sigma^2}$, as given by the Gaussian convolution theorem [17]. Note that we retrieve the original single photo-electron distribution in the case where $N = 1$.

Since the underamplified and the nominal components of the single-photo-electron distribution ought not to be entirely independent, we have opted to define μ_u and σ_u in terms of two scaling factors $0 < \zeta_G \leq 1$ and $0 < \zeta_\Sigma \leq 1$, such that:

$$\mu_u = \zeta_G \cdot G, \quad (21)$$

$$\sigma_u = \zeta_\Sigma \cdot \Sigma. \quad (22)$$

This way, when the gain or the gainspread of the PMT is adjusted, both parts of the single photo-electron distribution (as well as the resulting multi photo-electron distribution) will be affected. Assuming a Poissonian dynode response, where the spread in the final charge distribution is caused by statistical fluctuations in the first electron multiplication step, we can set $\zeta_G = \sigma_G^2$, such that $\mu_u = \Sigma^2$. Making sure that $\sigma_u \propto \sqrt{\mu_u}$, we subsequently set $\zeta_\Sigma = \sqrt{\zeta_G} = \sigma_G$.

4.1 Charge Distribution Lower Bound and Thresholdband

Due to application of a threshold, the domain of the charge distribution is bounded towards the lower end. In the past, this lower bound was presumed to be equal to the charge of a pulse which falls just short of the threshold setting, i.e. $q > q_0$. However, we observe an excess in the time-over-threshold distributions around 4 ns, which is incompatible with such an assumption. This time-over-threshold corresponds to the RC-time of the electronics [18]. It has been shown that this excess corresponds to genuine hits [19]. A possible explanation is given by a sub-threshold contribution of the analogue signal of the PMT. Hence, we include a part of the charge distribution which lies below the threshold from this point onwards.

The current version of J_{pp} accommodates an effective tuning of the lower domain-bound on the charge distribution using an additional parameter called the thresholdbandwidth, q_b . Any non-zero setting of this parameter will shift the lower bound to $q_0 - q_b$. The region of charge within $(q_0 - q_b) < q < q_0$ is correspondingly referred to as the thresholdband.

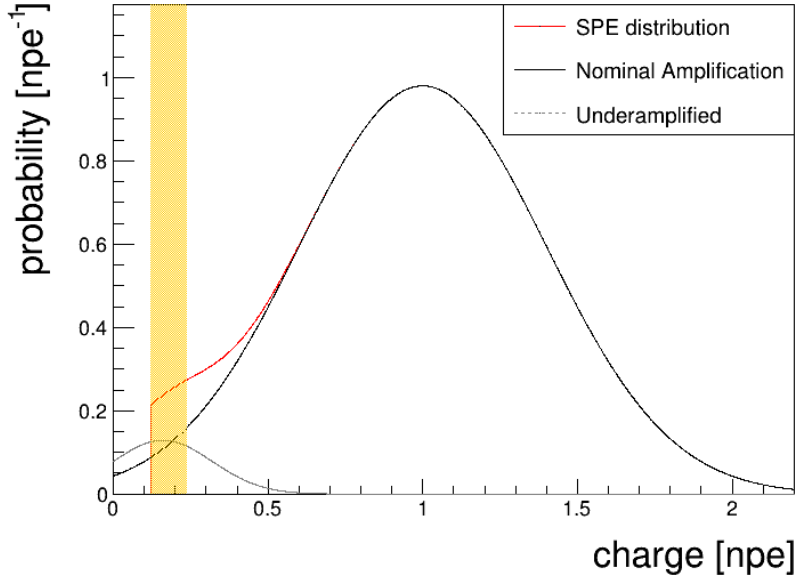


Figure 5: The single photo-electron distribution model for $p = 0.05$, $\zeta_G = \sigma_G^2 = 0.09$ and $\zeta_\Sigma = \sigma_G = 0.3$. The individual contributions from the underamplified and nominal charge distributions are indicated with the black dotted and solid lines, respectively. The area marked in orange shows the thresholdband.

In figure 5 the modeled single photo-electron distribution is shown. Note that the presence of the lower-bound effectively constitutes a truncation of the overall distribution. To ensure proper normalization, the sum in equation 20 should therefore be divided by a factor Q , given by:

$$\begin{aligned}
 Q &= \int_{q_0 - q_b}^{\infty} f(q; N) dq \\
 &= \frac{1}{2} \sum_{k=0}^N \binom{N}{k} p^{N-k} (1-p)^k \cdot \operatorname{erfc} \left(\frac{(q_0 - q_b) - \mu_k}{\sigma_k \sqrt{2}} \right), \tag{23}
 \end{aligned}$$

where $\operatorname{erfc}(z) = 1 - \operatorname{erf}(z) = \frac{2}{\sqrt{\pi}} \int_z^{\infty} e^{-t^2} dt$ denotes the complementary error function.

4.2 Sampling the charge distribution

To verify the parameter configuration used to describe a certain PMT, we often compare experimental data with simulations. This requires the generation of random data-samples using specific calibration settings. In Jpp, the former can be done by drawing random samples from a PMT's charge distribution. Since the charge distribution (c.f. equation 20) constitutes what is called a truncated mixture distribution, the generation of associated random variables requires two steps instead of one. The first step decides which of the contributions in the sum of equation 20 to draw from. Mathematically this winds down to a single sampling from a multinomial distribution with N categories, each category having an occurrence probability $p_j = \binom{N}{j} p^{N-j} (1-p)^j$. In other words, one needs to draw a single collection of random variables $(X_1, \dots, X_N) \sim \mathcal{M}(n = 1; p_1, \dots, p_N)$. Computationally, this can be accomplished via inversion sampling¹. Having drawn an auxiliary random variable Y from a uniform distribution, the multi photo-electron distribution component, k , for which $X_k = 1$ is given by:

$$k = \min \left\{ j \in \{1, \dots, N\} : \left(\sum_{i=1}^j p_i \right) \geq Y \right\}. \quad (24)$$

The second step draws a random charge-value from this component. This is done with ROOT, using the acceptance-complement ratio method for drawing from a standard normal (see W. Hoermann and G. Derflinger (1990) [20] for more information).

5 The survival probability

As seen in section 4, introducing the concept of underamplified hits modifies the shape of the charge distribution. Similarly, it affects the survival probability. This is defined as the chance that a specific number

¹This works because each of the random draws X_i has a marginal Bernoulli distribution: $X_i | X_{i-1}, \dots, X_1 \sim \mathcal{B}(n = 1; 1 - \sum_{k=1}^{i-1} X_k, p_i / (1 - p_{i-1}))$.

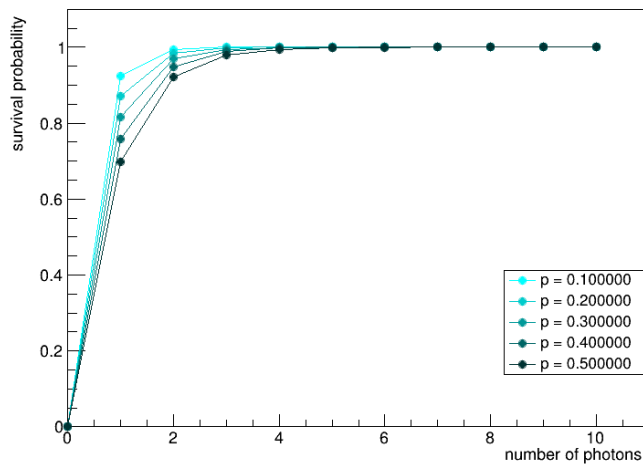


Figure 6: The survival probability of as a function of the number of photons impinging on the photocathode, for different settings of the underamplification probability, p .

of initial photons impinging on the photo-cathode generate a hit. Assuming that all photons would result in the emission of a primary photo-electron, we could simply evaluate it as:

$$\epsilon(N) \equiv \frac{\int_{q_0}^{\infty} f(q; N) dq}{\int_0^{\infty} f(q; N) dq}. \quad (25)$$

Here the influence of underamplification becomes apparent: the higher the underamplification probability p , the smaller the contribution of pulses with charge above the threshold. To simulate the detector response to Cherenkov light, it is convenient to introduce an additional average quantum efficiency $\langle \eta \rangle$ (c.f. section 2.1). The number of primary photo-electrons, n_p , generated by the photo-cathode due to the impingement of N photons, will then be distributed as a binomial. Consequently, the probability density for N photon hits, generating an observable pulse with charge q at the anode, becomes:

$$P_{\text{obs}}(q; N) = \sum_{m=1}^N \binom{N}{m} \cdot \langle \eta \rangle^m \cdot (1 - \langle \eta \rangle)^{N-m} \cdot f(q; m), \quad (26)$$

where we have substituted the expression for the multi photo-electron distribution from equation 20.

$$\begin{aligned} P_{\text{survival}}(N) &= \frac{\int_{q_0}^{\infty} P_{\text{obs}}(q, N) dq}{\int_0^{\infty} f(q; N) dq} \\ &= \sum_{m=1}^N \binom{N}{m} \cdot \langle \eta \rangle^m \cdot (1 - \langle \eta \rangle)^{N-m} \cdot \frac{\int_{q_0}^{\infty} f(q; m) dq}{\int_0^{\infty} f(q; m) dq}, \\ &= \sum_{m=1}^N \binom{N}{m} \cdot \langle \eta \rangle^m \cdot (1 - \langle \eta \rangle)^{N-m} \cdot \epsilon(m). \end{aligned} \quad (27)$$

The result obtained from equation 27 is shown in figure 6. As expected, the chance of survival decreases whenever p goes up. One of the applications where the equation comes into play, is in the calibration of the relative quantum-efficiency, $\langle \eta \rangle$. Since the function also depends on the gain and gainspread of the PMT, it is important to perform the gain-calibration first. This can be done using the time-over-threshold fitting routine implemented in Jpp (see section 6).

6 The time-over-threshold Distribution

In this section, the procedure to estimate the gain and the gainspread of a photomultiplier tube from the measured time-over-threshold distributions is presented. To relate the time-over-threshold distribution to the charge distribution, we have to perform a change of variables. For this purpose, one can use the fact that for a function $g : \mathbb{R} \rightarrow \mathbb{R}$ with inverse g^{-1} , the probability density function of $Y = g(X)$, where X is a random variable distributed as $f_X(x)$, is given by:

$$f_Y(y) = f_X(g^{-1}(y)) \left| \frac{d}{dy}(g^{-1}(y)) \right|. \quad (28)$$

Associating Y with the time-over-threshold, ΔT , and X with the charge, q , this yields:

$$f(\Delta T; N) = f(q(\Delta T); N) \cdot \frac{\partial q(\Delta T)}{\partial \Delta T}. \quad (29)$$

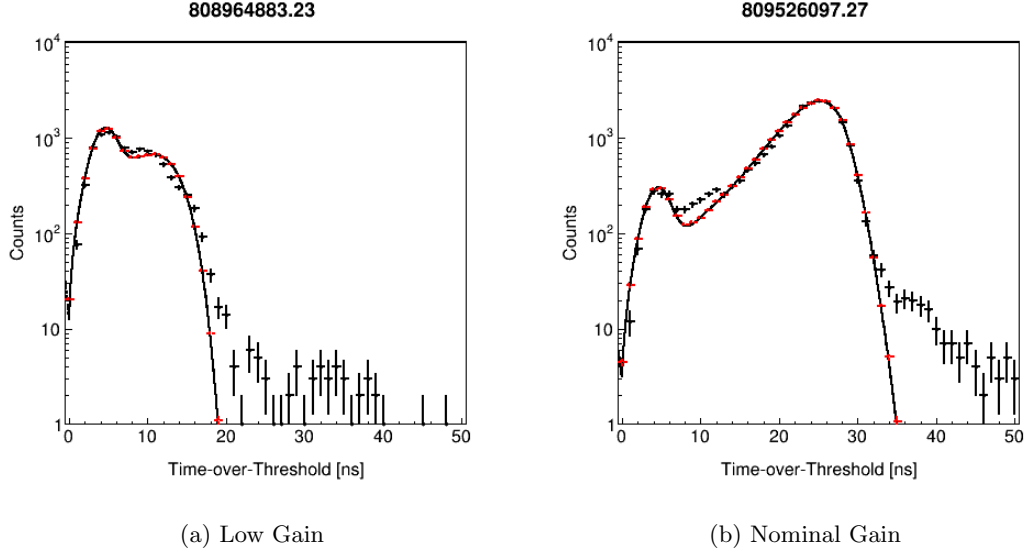


Figure 7: The time-over-threshold distributions retrieved for a low gain photomultiplier tube (a) and a photomultiplier tube with nominal gain (b) from the ORCA data corresponding to run number 6018. Black dots correspond to the original data and black solid lines to the result of a fit derived according to the model in equation 30, with $\mu_n = 4.5$ ns, $\sigma_n = 1.5$ ns, $q_0 = 0.22$ p.e., $q_b = 0.12$ p.e., $p = 0.05$, $\zeta_G = \sigma_G^2$ and $\zeta_\sigma = \sigma_G$. The red dots display simulation data generated with the model input obtained from the fit.

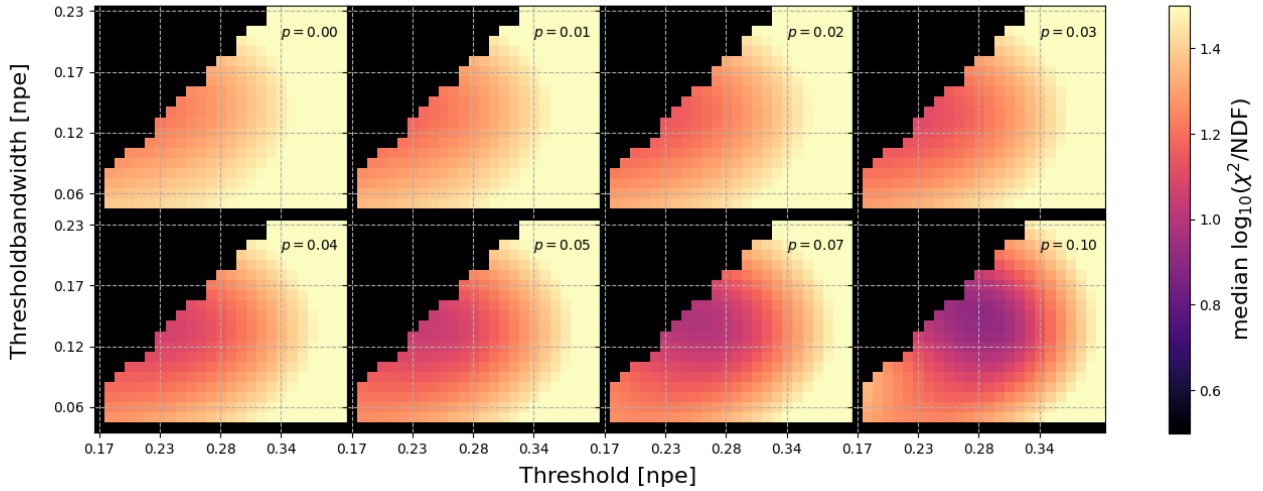


Figure 8: A gridscan over the parameter space relevant for fitting time-over-threshold distributions. The color scale displays the computed logarithmic median reduced chi-square over the fits of all time-over-threshold distributions which have been extracted from single coincident hit data (L1-data) in the 4-string ORCA run, 6018. The black areas indicate regions without data, deriving from the constraint that $q_b \leq q_0$. The images are arranged according to increasing underamplification probability, p , in top-to-bottom, left-to-right order.

As previously discussed in section 4.1, not all time-over-threshold measurements can be accounted for using the analytical pulseshape description given in section 3, because we observe an excess of pulses with time-over-thresholds around 4.5 ns. To account for the feature, we include an additional Gaussian distribution in equation 29, which scales according to the number of pulses with charge inside the thresholdband (c.f. section 4.1):

$$\begin{aligned} f(\Delta T; N) &= f_a(\Delta T) + f_b(\Delta T) \\ &= W_a \cdot f(q(\Delta T); N) \cdot \frac{\partial q(\Delta T)}{\partial \Delta T} + W_b \cdot \mathcal{G}(\Delta T; \mu_n, \sigma_n), \end{aligned} \quad (30)$$

where $\mu_n \approx 4.5$ ns and $\sigma_n \approx 1.5$ ns denote the mean and standard deviation of the observed excess. The normalization constants W_a and W_b are defined as $W_b = \int_{q_0 - q_b}^{q_0} f(q; N) dq$ and $W_a = 1 - W_b = \int_{q_0}^{\infty} f(q; N) dq$.

By varying over the gain and gainspread, implicitly contained through $f(q(\Delta T); N)$, we can use equation 30 to perform gain calibration with time-over-threshold data. Two time-over-threshold distributions are shown in figure 7. The original data points are indicated with black dots. A black curve presents the result of a fit obtained by varying equation 30 over the gain and gainspread. Additionally, the results of a simulation acquired using the derived fit parameters are shown in red.

Besides the gain and the gainspread, a number of other parameters are of influence on the outcome of the fit derived using equation 30. In an attempt to minimize the degrees of freedom, all of these parameters are fixed to a set value before the start of the fitting procedure. In figure 7, the chosen parameter values were $\mu_n = 4.5$ ns, $\sigma_n = 1.5$ ns, $q_0 = 0.33$ p.e., $q_b = 0.1$ p.e., $p = 0.05$. To understand which parameter settings yield optimal results, a gridscan was set up to iterate over different values of the thresholdband variables, q_0 and q_b , and of the underamplification probability, p , and calculate the reduced chi-square of the corresponding time-over-threshold fits. The results are shown in figure 8. Based on the reduced chi-square values, one might judge that a high setting of the underamplification probability greater than 0.05, yields the most reliable fit results. However, underamplification probabilities beyond the few percent level cannot be considered physical. Hence a trade-off has to be made between the setting of p and the width of the thresholdband, such that the effect of underamplification is not overestimated; we have chosen a default parameter configuration where $p = 0.05$, $q_0 = 0.24$ p.e. and $q_b = 0.12$ p.e., which comes with a median reduced chi-square of approximately $10^{1.1}$. The largest contribution to the chi-square for this setting is made by a second excess of pulses with time-over-threshold around 10 ns, which can be seen in both example distributions in figure 7. An additional, secondary thresholdband could be implemented in order to take this subpopulation into account. This has not yet been done.

7 Conclusion

In the previous sections we have presented an overview of the current photomultiplier tube response model implemented in Jpp, specifically the functions found within the classes JPMTSignalProcessorInterface

p	q_0 [p.e.]	q_b [p.e.]		$\langle \chi^2/\text{NDF} \rangle$
0.05	0.24	0.12		$10^{1.1}$

Table 1: The default parameter settings for the underamplification probability p , the threshold-equivalent charge q_0 and the thresholdbandwidth q_b , chosen to model the time-over-threshold distribution and the resulting median reduced chi-square of the fit results obtained for the ORCA data corresponding to run 6018.

and `JPMTAnalogueSignalProcessor`. Starting with the underlying working principles of the photomultiplier tube, we introduced the concepts of gain, gainspread, quantum efficiency and risetime in section 2. We then explored how these show up in the modeling of the pulse shape, charge distributions and in the time-over-threshold. In section 3 we showed how the photomultiplier pulses can be described using a Gaussian with an exponential tail. Such a definition leads to a direct, analytical formula for the time-over-threshold as function of charge. Together with the definition of the charge distribution, introduced in section 4, this formula allows for the derivation of the time-over-threshold probability density function (c.f. section 6), which can be used to fit the gain and gainspread from in-situ data, as explained in section 6. An excess around 4.5 ns (and 10 ns) in the time-over-threshold distributions has been observed. As shown in section 6, this can be taken into account by a sub-threshold contribution of the signal. An additional contribution to the lower end of the charge distribution from underamplification was introduced in order to account for the fraction of pulses observed within the thresholdband for photomultiplier tubes with nominal gain, as opposed to those with nominal gain. To reduce the number of degrees of freedom, all additional parameters needed for the model were fixed during the gain-fitting procedure. The optimal parameter settings were evaluated using a gridscan, which lead us to a default configuration where the probability of an underamplified hit is $p = 0.05$, the charge-equivalent threshold setting is $q_0 = 0.24$ p.e. and the width of the thresholdband is $q_b = 0.12$ p.e. (c.f. table 1).

While implementing the new concepts of the thresholdband and the phenomenon of underamplification, care was taken to make all changes compliant with already present functionalities. For example, the computation for the photon hit survival probability had to be modified in order to account for the dependence of the fraction of pulses with charge below the threshold on the chance of having underamplified hits (see section 5). Additionally, all modifications were carried out such that turning the newly added features off (i.e. setting $q_b = 0.0$ p.e. and $p = 0.0$), results in exactly the same computational behavior as before their implementation. All in all then, it can be said that the present PMT model implemented in `Jpp` allows for reproduction and fitting of photomultiplier tube time-over-threshold data, including the noisy feature seen around 4.5 ns, in a phenomenological and backwards-compatible way. For the future, the implementation of an additional thresholdband which models the additional peak around 10 ns might be considered.

References

- [1] *B.K. Lubsandorzhev. On the history of photomultiplier tube invention.* Nuclear Instruments and Methods in Physics Research Section A: Accelerators, Spectrometers, Detectors and Associated Equipment, *567(1):236 – 238, 2006. Proceedings of the 4th International Conference on New Developments in Photodetection.*
- [2] *KK Hamamatsu Photonics. Photomultiplier tube handbook.* Electron Tube Division,, *2006.*
- [3] *B. Herold, O. Kalekin, and J. Reubelt. Pmt characterisation for the km3net project.* Nuclear Instruments and Methods in Physics Research Section A: Accelerators, Spectrometers, Detectors and Associated Equipment, *639(1):70 – 72, 2011. Proceedings of the Seventh International Workshop on Ring Imaging Cherenkov Detectors.*
- [4] *AG Wright. The photomultiplier handbook.* Oxford University Press, *2017.*
- [5] *W. Shockley and J. R. Pierce. A theory of noise for electron multipliers.* Proceedings of the Institute of Radio Engineers, *26(3):321–332, March 1938.*
- [6] *Glenn F Knoll. Radiation detection and measurement(book).* New York, John Wiley and Sons, Inc., *1979. 831 p, 1979.*
- [7] *Philips Photonics. Photomultiplier tubes, principles and applications.* Philips Export BV, *1994.*

- [8] *Thijs Juan van Eeden. Measuring the Angular Acceptance of the KM3NeT Digital Optical Module. Master's thesis, Technische Universiteit Delft, the Netherlands, 2019.*
- [9] *L Baudis, S D'Amato, G Kessler, A Kish, and J Wulf. Measurements of the position-dependent photo-detection sensitivity of the hamamatsu r11410 and r8520 photomultiplier tubes. arXiv preprint arXiv:1509.04055, 2015.*
- [10] *S. Aiello, S.E. Akrame, F. Ameli, et al. Characterisation of the hamamatsu photomultipliers for the KM3net neutrino telescope. Journal of Instrumentation, 13(05):P05035–P05035, may 2018.*
- [11] *Bouke Jung. KM3NeT Computing and Software ELOG, message ID 444.*
- [12] *Jonas Reubelt. Hardware studies, in-situ prototype calibration and data analysis of the novel multi-pmt digital optical module for the km3net neutrino telescope. 2018.*
- [13] *E.H. Bellamy, G. Bellettini, J. Budagov, et al. Absolute calibration and monitoring of a spectrometric channel using a photomultiplier. Nuclear Instruments and Methods in Physics Research Section A: Accelerators, Spectrometers, Detectors and Associated Equipment, 339(3):468 – 476, 1994.*
- [14] *David J. Kissick, Ryan D. Muir, and Garth J. Simpson. Statistical treatment of photon/electron counting: Extending the linear dynamic range from the dark count rate to saturation. Analytical Chemistry, 82(24):10129–10134, 2010. PMID: 21114249.*
- [15] *J.R. Prescott. A statistical model for photomultiplier single-electron statistics. Nuclear Instruments and Methods, 39(1):173 – 179, 1966.*
- [16] *Pavel Degtiarenko. Precision analysis of the photomultiplier response to ultra low signals. Nuclear Instruments and Methods in Physics Research Section A: Accelerators, Spectrometers, Detectors and Associated Equipment, 872:115, Nov 2017.*
- [17] *Paul Bromiley. Products and convolutions of gaussian probability density functions. Tina-Vision Memo, 3(4):1, 2003.*
- [18] *Deepak Gajanaana. private communication.*
- [19] *Jannik Hofstaedt. KM3NeT Analysis ELOG, message ID 220.*
- [20] *W Hoermann and G Derflinger. The acr method for generating normal random variables. Operations-Research-Spektrum, 12(3):181–185, 1990.*